Science Foundation (SNSF), the National Center of Excellence in Research (NCCR) Structural Biology and RNA & Disease programs of the SNSF, European Research Council grant 250071 under the European Community's Seventh Framework Programme (to N.B.), the Commission of the European Communities through the PROSPECTS consortium (European Union FP7 projects 201648 and 233226) (R.A.), and the European Research Council (grant ERC-2008-AdG 233226) (R.A.). The 3.6 Å cryo-EM map of the 28S mitoribosomal subunit and the 3.8 Å cryo-EM map of the 55S mitoribosome have been deposited at the Electron Microscopy Data Bank (EMDB) with accession codes EMD-2913 and EMD-2914. Coordinates of the refined 28S subunit and the 55S mitoribosome in the canonical state have been deposited in the Protein Data Bank (PDB) with PDB codes 5AJ3 (28S) and 5AJ4 (55S). A PyMol script for display of the 55S mitoribosome is available from the Ban Lab website (www.mol.biol.ethz.ch/groups/ban_group/). ETH Zurich has filed a patent application to use the coordinates of the porcine mitoribosome structure for development of compounds that can (i) specifically interfere with mitochondrial translation by binding to mitoribosomes or (ii) specifically inhibit translation in pathogenic organisms without interfering with mitoribosomes.

SUPPLEMENTARY MATERIALS

www.sciencemag.org/content/348/6232/303/suppl/DC1
Materials and Methods
Supplementary Text
Figs. S1 to S10
Tables S1 to S7
References (*41*–*67*)
Data Table S1

27 November 2014; accepted 6 March 2015
10.1126/science.aaa3872

REPORTS

SURFACE STRUCTURE

Subatomic resolution force microscopy reveals internal structure and adsorption sites of small iron clusters

Matthias Emmrich,[1] Ferdinand Huber,[1] Florian Pielmeier,[1] Joachim Welker,[1] Thomas Hofmann,[1] Maximilian Schneiderbauer,[1] Daniel Meuer,[1] Svitlana Polesya,[2] Sergiy Mankovsky,[2] Diemo Ködderitzsch,[2] Hubert Ebert,[2] Franz J. Giessibl[1]*

Clusters built from individual iron atoms adsorbed on surfaces (adatoms) were investigated by atomic force microscopy (AFM) with subatomic resolution. Single copper and iron adatoms appeared as toroidal structures and multiatom clusters as connected structures, showing each individual atom as a torus. For single adatoms, the toroidal shape of the AFM image depends on the bonding symmetry of the adatom to the underlying structure [twofold for copper on copper(110) and threefold for iron on copper(111)]. Density functional theory calculations support the experimental data. The findings correct our previous work, in which multiple minima in the AFM signal were interpreted as a reflection of the orientation of a single front atom, and suggest that dual and triple minima in the force signal are caused by dimer and trimer tips, respectively.

The observation of "subatomic features" by atomic force microscopy (AFM) (*1*) in experiments where the front atom of the tip was imaged by the highly localized dangling bonds of the Si(111)-(7x7) surface atoms (*2*) raised discussions within the community (*3*). Similar observations were reported later for Si adatoms imaging Si tips (*4*), CoSm tips (*5*), and even in scanning tunneling microscopy (STM) (*6*). The initial results were obtained at room temperature, where the atomic configuration of the tip changes frequently. The stability offered at liquid helium temperatures allowed to resolve small features in tip images spaced by merely 77 pm (0.77 Å) (*7*). Again, the front atom of the tungsten tip was imaged by a sample consisting of light and small atoms (carbon in graphite) (*7*). Later, we used CO molecules to establish the COFI technique (carbon monoxide front atom identification) (*8*, *9*), building on expertise with CO imaging when measuring the forces that act during atomic manipulation (*10*). The adsorption geometry of CO molecules on Cu(111) surfaces is critical for the effectiveness of COFI: CO adsorbs perpendicular to Cu(111), with the C atom sitting on top of a Cu surface atom (*11*).

However, the purpose of microscopy is to image a sample, not to inspect the tip, so it was important to design well-defined tips with front atoms much smaller than typical metals. Gross *et al*. created such a sharp and well-defined tip by adsorbing a CO molecule to the metal tip, demonstrating submolecular (*12*) resolution on pentacene (*13*) and other molecules by AFM with a resolution that exceeds STM. The CO molecule attaches to the tip with the carbon atom, and the front atom of the tip is an oxygen atom. Tip functionalization by adsorbing a CO molecule on a metal tip had been introduced in STM before (*14*), but the dramatic increase in AFM resolution on organic matter was not foreseen and is used widely now—for example, to determine bond order (*15*) and chemical reaction products (*16*). The use of CO-terminated metal tips enabled reversing the experiment (*8*) and imaging single atoms in various bonding configurations to check whether subatomic resolution (*12*) is possible on a sample. Here, we first analyze the imaging of single adatoms and then expand to image small clusters.

The contrast for CO tips at small distances arises from Pauli repulsion forces that increase with charge density (*17*), similar to the interaction of closed-shell atoms with molecules (*18*). Pauli repulsion allows for a descriptive interpretation where the AFM image represents the charge density that is maximal on top of atoms—in contrast to STM, which maps the charge density at the Fermi level. However, the CO molecule bonded to the metal tip easily bends laterally (*13*, *19*), and artifacts such as lateral distortions, apparent bond lengthening, bond sharpening, and cusplike maxima within aromatic rings must be anticipated [see figure 1 in (*15*)]. Thus, we first checked the imaging characteristics of CO tips for adatoms using silicon, with its well-known structure.

A CO-terminated tip created AFM images of the Si(111)-(7x7) reconstruction (Fig. 1A) that clearly display the 12 adatoms and even the 6 rest atoms in each unit cell. Adatoms and rest atoms hybridize into four $3sp^3$ orbitals, where the orbitals normal to the surface appear as roughly Gaussian protrusions. The calculated charge density of Si(111)-(7x7) (Fig. 1B) is similar to the experimental image in Fig. 1A. Figure 1B shows the charge density of the protruding $3sp^3$ orbitals, and Fig. 1C (experimental) and Fig. 1D (calculated) focus on a single Si adatom. The density calculations of Fig. 1 use Slater-type orbitals (STO) (*20*), with details for Si in (*4*) and in (*9*) for the following metallic adatoms.

Figure 1E is an AFM image of a single Cu adatom on a Cu(111) surface. Surprisingly, the Cu adatom does not appear as a single protrusion like the Si adatom in Fig. 1C but shows a toroidal structure. We postulate that the origin of this toroidal shape is in the electronic configuration of the adatom. Figure S1 (*21*) shows the contrast development for the Cu adatom with distance: For larger distances, the adatom appears attractive (fig. S1A); for an intermediate distance, a repulsive ring appears (fig. S1B); finally, for very close distances, artifacts from CO bending (which have also been seen when imaging organic molecules) appear in which the repulsive ring becomes sharper (fig. S1C) and a repulsive center cusp starts to emerge (fig. S1D). The electronic configuration of a neutral Cu atom is $[Ar]3d^{10}4s^1$. Fully occupied subshells as well as the 4s electron of a free Cu atom yield a spherically symmetric charge density. However, the Smoluchowski effect (*22*) leads to a positive charge of protruding

[1]Institute of Experimental and Applied Physics, Department of Physics, University of Regensburg, 93053 Regensburg, Germany. [2]Department Chemie, Ludwig-Maximilians-Universität München, Butenandtstrasse 11, 81377 München, Germany.
***Corresponding author. E-mail: franz.giessibl@ur.de**

surface features such as steps or adatoms, surrounded by a surplus in negative charge. Imaging the polar surface of Cu_2N with a CO-terminated tip has revealed that the CO-terminated tip forms a dipole with the negative end at the oxygen atom (*23*), in agreement with density functional theory (DFT) calculations (*24*, *25*) and similar to CO adsorbed on several (111) metal surfaces (*11*).

Thus, the toroidal symmetry of the experimental image of a Cu adatom shown in Fig. 1E arose from electrostatic attraction at the center and Pauli repulsion at the circumference. The charge redistribution created by the Smoluchowski effect can be mapped on atomic states by a hybridization of |4s> into a $(|4s\rangle-|4p_z\rangle)/\sqrt{2}$ state. Figure 1F shows the calculated charge density of this state with STO orbitals, and the inset shows the charge gradient in the *z* direction using DFT. The calculation of the interaction of CO-terminated tips with adatoms and clusters is still too complex for the current status of DFT, so we use H and Xe atoms as tip models in DFT calculations. Given that the highest occupied states within bulk copper have a bonding energy of ~5 eV, perturbation theory yields an energetic lowering of the |4s> state when hybridizing into a $(|4s\rangle-|4p_z\rangle)/\sqrt{2}$ state. This process would also explain why a Cu adatom with its diameter of 255 pm has a much lower apparent height of ~100 pm in STM. We note that these toroidal symmetries have been observed before in the reverse situation, where a CO molecule adsorbed on Cu(111) probed the metallic tip atom [see figure 1D in (*8*); figure 1, c and h, in (*9*); and figure 1D in (*10*)].

Figure 1G shows a Cu adatom on a Cu(110) surface. The (110) surface has a twofold symmetry, and the toroidal image of the Cu adatom has two dips in it, according to the twofold symmetry of the substrate. It can be modeled in the STO-based charge density by a 2% mixing of a $|4p_y\rangle$ orbital into the $(|4s\rangle-|4p_z\rangle)/\sqrt{2}$ state as calculated in Fig. 1H.

Figure 1I is an AFM image of an Fe adatom on Cu(111). A free Fe atom has an electronic configuration of $[Ar]3d^64s^2$. Similar to the Cu adatom, it shows an overall toroidal structure, and it is centered around a face-centered-cubic (fcc) site (see fig. S2). However, the torus has three bumps that point to the three next-nearest Cu atoms of the substrate. Figure 1J is an STO-type charge calculation with a $4sp_z$ hybridization. Possibly, further hybridization with electrons from the unfilled 3d states occurs that could explain the three bumps on the torus-shaped image. The overall toroidal shape with a threefold symmetry of the Fe adatom interacting with a Xe tip is revealed by DFT using the Vienna Ab-initio Simulation Package (VASP) code (*26*) (inset of Fig. 1J and fig. S3). The possibility of detecting subatomic contrast has been discussed previously based on DFT calculations by Huang *et al.* (*27*) and Zotti *et al.* (*28*) for silicon and Wright and Solares (*29*) for tungsten. Figure 1K is an AFM image of an Fe atom on an Fe island. Its threefold symmetry is explained by the contribution of 3d states, as shown in Fig. 1L after the calculations published in figure S10 of (*9*).

Although atoms can be positioned with atomic precision by STM, their exact location is determined by the chemical bonds that develop. Because Cu(111) appears flat in STM under normal tunneling conditions, adsorption-site determination by STM is difficult. Brune *et al.* (*30*) used STM at low bias and high current to resolve the surface lattice and adsorption site of C on aluminum(111). Repp *et al.* (*31*) used STM and atomic manipulation (*32*) to determine that single Cu adatoms on a Cu(111) surface preferably adsorb at fcc sites, under the assumption that stripes of Cu adatoms also adsorb on fcc sites. Stroscio and Celotta (*33*) have identified fcc sites as the preferred adsorption sites of Co atoms on Cu(111) by monitoring the fluctuations of the tunneling current during atomic manipulation. In the well-known quantum corral experiment, 48 Fe atoms were arranged in a circle on Cu(111) by atomic manipulation by STM (*34*). The adsorption site was not determined in the quantum corral, but evidence was found later that Fe adatoms preferentially adsorb on fcc sites (*35*).

Figure 2A shows an STM image of a dimer, Fig. 2E of a trimer, and Fig. 2I of a tetramer, recorded with a metal tip. In agreement with previous reports (*36*, *37*), STM only reveals single roughly Gaussian peaks where the height depends on the number of atoms (see fig. S4). It has been observed before [figure 2 in (*8*)] that differential STM data or Laplace filtering of STM data recorded with CO-terminated tips partially reveals the highly resolved AFM data.

AFM with CO tips could directly image the Cu(111) surface lattice (*38*), so adsorption sites of Fe adatoms and clusters can be determined by centering a lattice overlay that registers with the Cu atom surface layer as in Fig. 2, C, G, and K. Although CO tip-bending artifacts lead to an apparent larger lateral size of clusters, the AFM images allow conclusions about the adsorption sites. Given that Fe monomers preferentially adsorb on fcc sites, one would assume that the two Fe atoms comprising a dimer also adsorb on fcc. However, the AFM image of the dimer in Fig. 2, B and C, does not share the symmetry of the surface. Although some of that asymmetry might be caused by a slight tilt in the CO tip molecule, DFT calculations in fig. S5 predict an asymmetric adsorption with adsorption sites near two next-nearest bridge sites, as displayed in Fig. 2D.

Trimers adsorb in three different geometries. The most prevalent adsorption symmetry is shown in Fig. 2, F and G. This trimer is centered on top

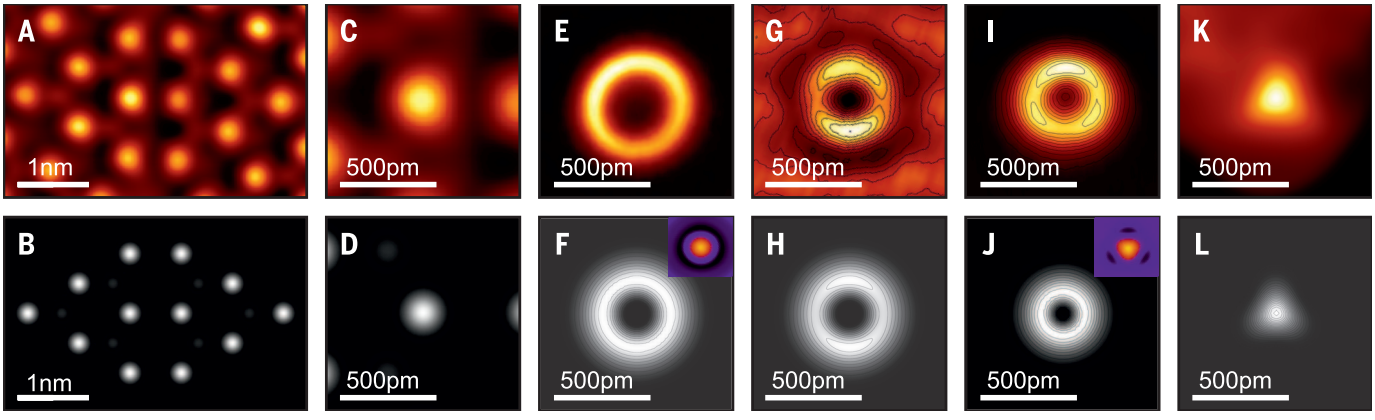

Fig. 1. Constant-height mode AFM images (top row) and simulations (bottom row) of silicon, copper, and iron surface atoms. (**A**) AFM image of the Si(111)-(7x7) reconstruction using a CO-terminated metal tip. The rest atoms are clearly visible. (**B**) Calculated valence charge density of Si(111)-(7x7) reconstruction, using Slater-type orbitals as discussed in (*4*). (**C**) Magnified view of a single adatom (center-faulted half). (**D**) Calculated charge density of that atom. (**E**) Experimental AFM image of a Cu adatom on Cu(111), showing a ringlike symmetry that is caused by a toroidal charge density of the adatoms. (**F**) Calculated charge density of the Cu adatom using a $4sp_z$ hybrid state (*21*). The inset shows the charge gradient calculated with DFT (see fig. S3D). (**G**) Experimental image of a Cu adatom on a Cu(110) surface. (**H**) Calculated charge density of the Cu adatom using a $4sp_z$ hybrid state plus a $4p_y$ state (*21*). (**I**) Experimental AFM image of a Fe adatom on Cu(111), showing the Fe adatom as a torus with three local maxima. (**J**) Calculated charge density of the Fe adatom on Cu(111) using a $4sp_z$ hybrid state. The inset shows the charge gradient calculated with DFT (see fig. S3E). (**K**) Experimental AFM image of an Fe adatom on an Fe island. (**L**) Simulated AFM image according to supplemental figure S10 in (*9*).

of a Cu atom, with the Fe atoms adsorbed near bridge sites pointing toward the nearest neighbors of the center atom. For this bonding geometry, two orientations exist, and they can be rotated by the AFM tip, as displayed in fig. S6. DFT confirms that the bridge-site adsorption geometry is energetically favorable over an fcc site geometry for trimers that are centered on top of a Cu atom (fig. S7). Experimentally, we also find a second type of trimer centered around a hexagonal close-packed (hcp) site (see fig. S8). DFT confirms that this trimer has an even lower adsorption energy (fig. S7A). Because of the symmetry of the surface lattice, a trimer centered on an hcp site with Fe atoms on fcc sites can only point in one orientation, with the three Fe atoms sitting on fcc sites. Experimentally, we only found hcp-centered trimers that show a triangle that pointed downward, as displayed in fig. S8. Unlike the bridge-site trimer, it was not possible to rotate or move the fcc-site trimer. A third type of trimer is depicted in fig. S9A. The Laplace-filtered version of it in fig. S9B shows that there is a mirror axis, but it is not possible to assign atomic positions from the data. Possibly, this orientation involves a dynamic state. The identity of these structures as trimers was verified by manipulating an additional Fe atom to them, yielding a stable tetramer, as displayed in Fig. 2J. For tetramers (Fig. 2J) and larger clusters discussed below, the iron atoms apparently adsorb on fcc sites.

Figure 3A shows AFM images of two large Fe clusters. The right cluster is composed of 16 atoms, with 15 atoms on the Cu(111) substrate and one atom on top. The left cluster is built from 12 atoms, with one atom on the top of the island. This top atom moved during imaging and appeared as a streak; it did not move in a consecutive fast scan of the same two clusters shown in fig. S13. Figure 3B is a Laplace-filtered version of Fig. 3A, and Fig. 3C includes a lattice overlay. The central parts of the clusters show that for large clusters, the Fe atoms are located on fcc sites. The edges of the clusters appear strongly distorted, similar to the distortions in edges of pentacene and other organic molecules (*13*, *15*). Resolving the structure of small clusters should prove to be useful in many fields—for example, in nanomagnets, where the structure of Fe clusters influences their magnetic properties (*37*).

The initial goal of the present experiments was to achieve subatomic spatial resolution of AFM by reversing the experiment of (*8*), in which COFI images of tungsten tips similar to Fig. 2B were interpreted as single atom tips oriented in a [110] crystal direction, and COFI images similar to Fig. 2F were thought to originate from a single atom tip oriented in a [111] direction. We found that COFI images of Fe with its body-centered-cubic (bcc) structure are similar to COFI images of tungsten (also bcc) [see figure S4 in (*39*)]. It is easier to evaporate Fe on Cu(111) than W because of its lower melting point. Thus, we compared constant-height AFM images that use a CO tip to image Fe dimers and trimers with the constant-height COFI images of Fe tips with dual and triple minima in figs. S10 and S11, respectively. The similarity in force values, lateral extent, and appearance is excellent, so we conclude that the interpretation of tips 2 and 3 as pointing in a [110] and [111] direction in (*8*) is incorrect. Rather, we conclude that tips 2 and 3 were dimer and trimer tips, respectively (*40*).

Constant-height AFM images of dimers showed two local minima separated by a repulsive barrier (fig. S10), and trimers showed a starlike structure (fig. S11). Figure S12 shows the square of a superposition of two (fig. S12A) and three (fig. S12B) $4sp_z$ states that were centered on two and three Cu atoms. Qualitatively, this charge density calculated from the square of $4sp_z$ states is similar to the experimental constant-height images, which suggests that the $4sp_z$ states are important for bonding the clusters. The interplay of internal cluster bonding and bonding to the substrate allows manipulation for some clusters (fig. S6), and second-layer atoms on clusters (Fig. 3 and fig. S13) pose an interesting challenge for theory and experiment in catalysis and surface science in general.

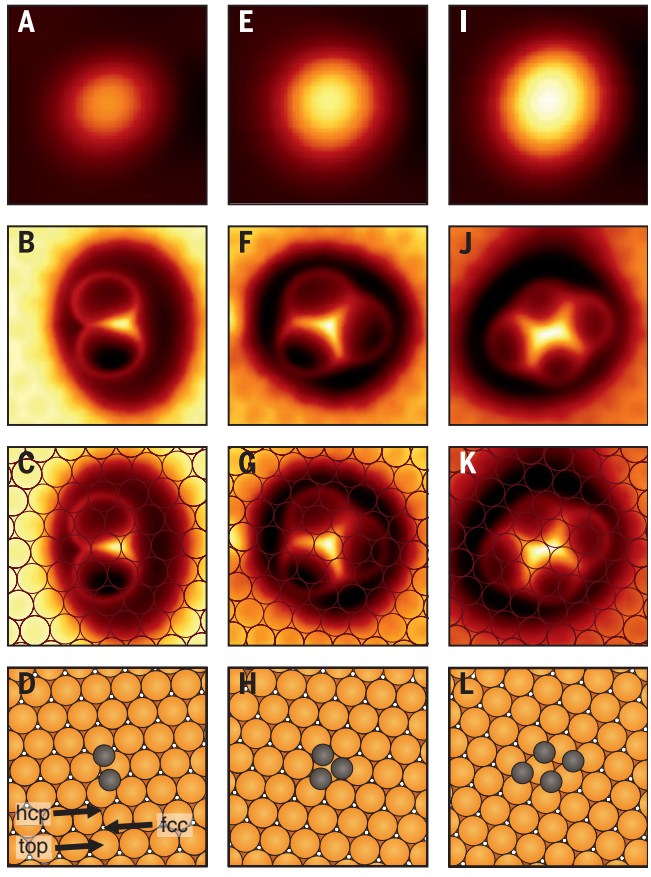

Fig. 2. Dimers, trimers, and tetramers imaged by STM, AFM, and their calculated adsorption sites. The first row shows constant-current STM data using a metal tip [(**A**), (**E**), and (**I**)] of an Fe dimer on Cu(111) (left column), Fe trimer (center column), and Fe tetramer (right column). The second row [(**B**), (**F**), and (**J**)] shows the AFM signal (frequency shift) recorded in constant-current topographic imaging with a CO-terminated tip. The dark spots in the flat regions correspond to Cu surface atoms that allow us to register the lattice overlay in the third row [(**C**), (**G**), and (**K**)]. The last row [(**D**), (**H**), and (**L**)] shows the proposed adsorption sites, indicating top, fcc, and hcp positions. An adatom centered on a fcc site thus continues the bulk fcc structure, whereas an adatom on a hcp site would break the crystalline order of the fcc bulk. DFT calculations (*21*) reveal that dimers (D) adsorb with the two Fe atoms close to two next-nearest bridge sites. On-top centered trimers (H) also adsorb with the three Fe atoms close to bridge sites, and tetramers (L) adsorb on fcc sites. The top row and the rows below show different clusters.

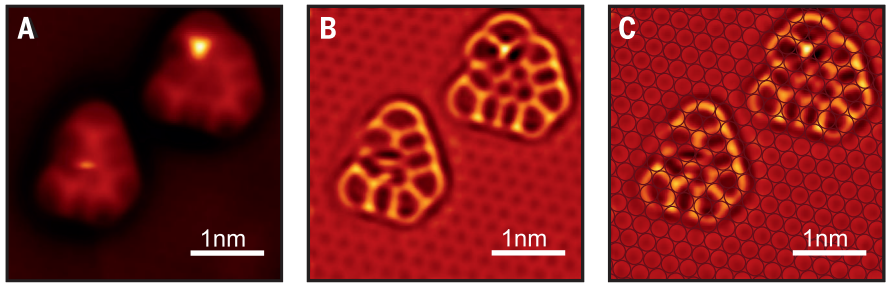

Fig. 3. Images of two nearby Fe clusters. (**A**) AFM image of two nearby Fe clusters. (**B**) Double Laplace-filtered image of (A). (**C**) Same image as (B), including a lattice overlay that shows the adsorption geometry. Both clusters have an additional atom on top; this atom has moved during scanning in the left cluster. The edges of the clusters appear strongly distorted because of CO bending; the center parts show that the Fe adatoms comprising the cluster adsorb on fcc sites.

REFERENCES AND NOTES

1. G. Binnig, C. F. Quate, C. Gerber, *Phys. Rev. Lett.* **56**, 930–933 (1986).
2. F. J. Giessibl, S. Hembacher, H. Bielefeldt, J. Mannhart, *Science* **289**, 422–425 (2000).
3. H. J. Hug *et al.*, *Science* **291**, 2509a (2001).
4. F. J. Giessibl, H. Bielefeldt, S. Hembacher, J. Mannhart, *Ann. Phys.* **10**, 887–910 (2001).
5. M. Herz, F. J. Giessibl, J. Mannhart, *Phys. Rev. B* **68**, 045301 (2003).
6. A. N. Chaika, A. N. Myagkov, *J. Phys. Conf. Ser.* **100**, 012020 (2008).
7. S. Hembacher, F. J. Giessibl, J. Mannhart, *Science* **305**, 380–383 (2004).
8. J. Welker, F. J. Giessibl, *Science* **336**, 444–449 (2012).
9. T. Hofmann, F. Pielmeier, F. J. Giessibl, *Phys. Rev. Lett.* **112**, 066101 (2014).
10. M. Ternes, C. P. Lutz, C. F. Hirjibehedin, F. J. Giessibl, A. J. Heinrich, *Science* **319**, 1066–1069 (2008).
11. A. Zangwill, *Physics on Surfaces* (Cambridge Univ. Press, Cambridge 1988).
12. Submolecular resolution is defined as the ability to resolve atomic positions within molecules. Here, we refer to subatomic resolution as the ability to image single atoms as nontrivial features such as tori or multiple extrema, in contrast to single protrusions or single depressions.
13. L. Gross, F. Mohn, N. Moll, P. Liljeroth, G. Meyer, *Science* **325**, 1110–1114 (2009).
14. L. Bartels, G. Meyer, K. H. Rieder, *Appl. Phys. Lett.* **71**, 213 (1997).
15. L. Gross *et al.*, *Science* **337**, 1326–1329 (2012).
16. D. G. de Oteyza *et al.*, *Science* **340**, 1434–1437 (2013).
17. N. Moll, L. Gross, F. Mohn, A. Curioni, G. Meyer, *New J. Phys.* **12**, 125020 (2010).
18. R. G. Gordon, Y. S. Kim, *J. Chem. Phys.* **56**, 3122 (1972).
19. A. J. Weymouth, T. Hofmann, F. J. Giessibl, *Science* **343**, 1120–1122 (2014).
20. J. C. Slater, *Phys. Rev.* **36**, 57–64 (1930).
21. Supplementary materials are available on *Science* Online.
22. R. Smoluchowski, *Phys. Rev.* **60**, 661–674 (1941).
23. M. Schneiderbauer, M. Emmrich, A. J. Weymouth, F. J. Giessibl, *Phys. Rev. Lett.* **112**, 166102 (2014).
24. M. Feng *et al.*, *ACS Nano* **5**, 8877–8883 (2011).
25. P. Hapala, R. Temirov, F. S. Tautz, P. Jelínek, *Phys. Rev. Lett.* **113**, 226101 (2014).
26. G. Kresse, J. Hafner, *Phys. Rev. B* **47**, 558–561 (1993).
27. M. Huang, M. Čuma, F. Liu, *Phys. Rev. Lett.* **90**, 256101 (2003).
28. L. A. Zotti, W. A. Hofer, F. J. Giessibl, *Chem. Phys. Lett.* **420**, 177–182 (2006).
29. C. A. Wright, S. D. Solares, *Nano Lett.* **11**, 5026–5033 (2011).
30. H. Brune, J. Wintterlin, G. Ertl, R. J. Behm, *Europhys. Lett.* **13**, 123–128 (1990).
31. J. Repp, G. Meyer, K.-H. Rieder, P. Hyldgaard, *Phys. Rev. Lett.* **91**, 206102 (2003).
32. D. M. Eigler, E. K. Schweizer, *Nature* **344**, 524–526 (1990).
33. J. A. Stroscio, R. J. Celotta, *Science* **306**, 242–247 (2004).
34. M. F. Crommie, C. P. Lutz, D. M. Eigler, *Science* **262**, 218–220 (1993).
35. A. Biedermann, W. Rupp, M. Schmid, P. Varga, *Phys. Rev. B* **73**, 165418 (2006).
36. M. Pivetta, G. E. Pacchioni, U. Schlickum, J. V. Barth, H. Brune, *Phys. Rev. Lett.* **110**, 086102 (2013).
37. A. A. Khajetoorians *et al.*, *Science* **339**, 55–59 (2013).
38. B. Schuler *et al.*, *Phys. Rev. Lett.* **111**, 106103 (2013).
39. F. Pielmeier, F. J. Giessibl, *Phys. Rev. Lett.* **110**, 266101 (2013).
40. Our initial experiments of evaporating Fe atoms on Cu(111) appeared to confirm the findings of the inverse of the threefold tip 3 of (*8*), because we found many threefold structures that we first misinterpreted as single atoms. It turned out that upon extended Fe evaporation, the copper crystal heated up to ~15 K and the Fe monomers became mobile enough to form an abundance of trimers.

ACKNOWLEDGMENTS

We thank G. Binnig, J. Repp, and A. J. Weymouth for discussions and the Deutsche Forschungsgemeinschaft for funding under Graduiertenkolleg 1570 and Sonderforschungsbereich 689, as well as M. Grifoni (speaker of GRK) and D. Weiss (speaker of SFB) for support. F.J.G. thanks A. Heinrich for hosting several visits at the IBM Almaden Research Center from 2005 until 2010, where first attempts to resolve metallic adatoms with subatomic resolution were performed together with C. Lutz, C. Hirjibehedin, and M. Ternes. Author contributions: M.E. performed most of the measurements and data analysis, constructed the low-temperature scan head, and prepared most figures; F.H. optimized the electronics and performed crucial measurements; J.W. performed measurements on Cu adatoms on Cu(111); T.H. and F.P. performed measurements on Cu/Cu(110) and inverse measurements using CO/Cu(111) to characterize Cu and Fe tips; M.S. constructed most of the vacuum system and sample-preparation facilities; D.M. performed the AFM measurements on Si; D.K., S.P., S.M., and H.E. performed the DFT calculations; and F.J.G. initiated and directed the project, employed the STO model, and wrote the manuscript.

SUPPLEMENTARY MATERIALS

www.sciencemag.org/content/348/6232/308/suppl/DC1
Materials and Methods
Supplementary Text
Figs. S1 to S13
References (*41*–*47*)

19 December 2014; accepted 20 February 2015
Published online 19 March 2015;
10.1126/science.aaa5329

ACTIVE GALAXIES

A strong magnetic field in the jet base of a supermassive black hole

Ivan Martí-Vidal,* Sébastien Muller, Wouter Vlemmings, Cathy Horellou, Susanne Aalto

Active galactic nuclei (AGN) host some of the most energetic phenomena in the universe. AGN are thought to be powered by accretion of matter onto a rotating disk that surrounds a supermassive black hole. Jet streams can be boosted in energy near the event horizon of the black hole and then flow outward along the rotation axis of the disk. The mechanism that forms such a jet and guides it over scales from a few light-days up to millions of light-years remains uncertain, but magnetic fields are thought to play a critical role. Using the Atacama Large Millimeter/submillimeter Array (ALMA), we have detected a polarization signal (Faraday rotation) related to the strong magnetic field at the jet base of a distant AGN, PKS 1830–211. The amount of Faraday rotation (rotation measure) is proportional to the integral of the magnetic field strength along the line of sight times the density of electrons. The high rotation measures derived suggest magnetic fields of at least tens of Gauss (and possibly considerably higher) on scales of the order of light-days (0.01 parsec) from the black hole.

The AGN jets, related to the accretion mechanism in supermassive black holes, consist of relativistic plasma driven by strong and ordered magnetic fields. As a result of the magnetic interaction of the plasma, nonthermal (synchrotron) emission is produced (*1*). Studying the polarization of this nonthermal emission from AGN is a direct way to probe the structure and strength of magnetic fields in the vicinity of a black hole. Of particular importance is the observation of the rotation measure, *RM*, defined as the change of polarization angle as a function of wavelength squared. This quantity is directly related to the plasma density and the strength of the magnetic field along the line of sight.

To date, it has been extremely difficult to obtain accurate polarimetric information from the innermost (subparsec) regions of AGN; only emission at submillimeter wavelengths can escape from these regions, due to a large synchrotron self-absorption (SSA) that blocks the emission at longer wavelengths. Unfortunately, the sensitivity of polarization observations at submillimeter wavelengths has so far been strongly limited by the instrumentation.

Previous attempts to detect Faraday rotation at submillimeter (submm) wavelengths from AGN have yielded only upper limits (*2*, *3*) and marginal detections (*4*) that require strong assumptions about the absence of variability on time scales of weeks. There is a more robust detection for the Galactic center (*5*), although the activity in this source is much lower than in AGN. Recently, measurements of Faraday rotation in the nearby AGN 3C 84 (redshift $z = 0.018$) have been reported at mm wavelengths (*6*).

We have obtained measurements of Faraday rotation at frequencies up to 300 GHz (about 1 THz in the rest frame of the source) from PKS 1830–211, a powerful gravitationally lensed AGN located at a redshift of $z = 2.5$ (*7*). At these frequencies, SSA is negligible in the whole jet of PKS 1830–211 (*8*), and the maximum emission originates at the jet region closest to the black hole; the zone where the plasma is being injected and accelerated into the main jet stream. At lower frequencies, SSA hides this jet acceleration zone

Department of Earth and Space Sciences, Chalmers University of Technology, Onsala Space Observatory, SE-43992, Onsala, Sweden.
***Corresponding author. E-mail: mivan@chalmers.se**